Weierstraß-Institut

für Angewandte Analysis und Stochastik

Leibniz-Institut im Forschungsverbund Berlin e. V.

Preprint ISSN 2198-5855

Modeling of current spreading in high-power broad-area lasers and its impact on the lateral far field divergence

Anissa Zeghuzi[1], Mindaugas Radziunas[2], Hans Wenzel[1], Hans-Jürgen Wünsche[1,2], Uwe Bandelow[2], Andrea Knigge[1]

submitted: March 7, 2018

[1] Ferdinand-Braun-Institut
Leibniz Institut für Höchstfrequenztechnik
Gustav-Kirchhoff-Straße 4
12489 Berlin
Germany
E-Mail: anissa.zeghuzi@fbh-berlin.de
hans-juergen.wuensche@fbh-berlin.de
hans.wenzel@fbh-berlin.de
andrea.knigge@fbh-berlin.de

[2] Weierstrass Institute
Mohrenstr. 39
10117 Berlin
Germany
E-Mail: mindaugas.radziunas@wias-berlin.de
hans-juergen.wuensche@wias-berlin.de
uwe.bandelow@wias-berlin.de

No. 2488
Berlin 2018

2010 *Mathematics Subject Classification.* 78A60, 35Q60, 78M34, 78-04.

2010 *Physics and Astronomy Classification Scheme.* 42.55.Px, 02.30.Jr, 02.60.Lj.

Key words and phrases. High-power diode laser, current spreading, current modeling, lateral far-field.

This work is supported by the German Federal Ministry of Education and Research contract 13N14005 as part of the EffiLAS/HotLas project.

Edited by
Weierstraß-Institut für Angewandte Analysis und Stochastik (WIAS)
Leibniz-Institut im Forschungsverbund Berlin e. V.
Mohrenstraße 39
10117 Berlin
Germany

Fax: +49 30 20372-303
E-Mail: preprint@wias-berlin.de
World Wide Web: http://www.wias-berlin.de/

Modeling of current spreading in high-power broad-area lasers and its impact on the lateral far field divergence

Anissa Zeghuzi, Mindaugas Radziunas, Hans Wenzel, Hans-Jürgen Wünsche,
Uwe Bandelow, Andrea Knigge

Abstract

The effect of current spreading on the lateral far–field divergence of high–power broad–area lasers is investigated with a time–dependent model using different descriptions for the injection of carriers into the active region. Most simulation tools simply assume a spatially constant injection current density below the contact stripe and a vanishing current density beside. Within the drift–diffusion approach, however, the injected current density is obtained from the gradient of the quasi–Fermi potential of the holes, which solves a Laplace equation in the p–doped region if recombination is neglected. We compare an approximate solution of the Laplace equation with the exact solution and show that for the exact solution the highest far–field divergence is obtained. We conclude that an advanced modeling of the profiles of the injection current densities is necessary for a correct description of far–field blooming in broad–area lasers.

1 INTRODUCTION

Diode lasers provide an efficient possibility to convert electrical into optical energy. Due to their laterally wide emission stripe, broad–area (BA) lasers can achieve the highest output power among diode lasers and are therefore used as energy source for many laser systems and can also be employed for direct material processing. For many applications, however, not only a high output power but also a good beam quality is required. The beam quality is typically specified by the beam parameter product $\mathrm{BPP}_{\mathrm{lat}} = w_{95\%}\Theta_{95\%}/4$, where $w_{95\%}$ denotes the full lateral near–field width and $\Theta_{95\%}$ the full far field angle containing 95% of the power.

With rising current a broadening of the lateral far field is visible, which is the result of an increased excitation of higher order lateral modes with higher far field angles [1]. This phenomenon can be partly attributed to self–heating (thermally far–field blooming [2, 3, 4]) and the resulting thermal–induced waveguide by modification of the refractive index and partly to non–thermal effects (non–thermal far–field blooming [5]). Non–thermal far field blooming is a result of current spreading [5], lateral carrier diffusion and accumulation [6] and longitudinal and lateral spatial hole burning. Current spreading and lateral carrier diffusion and accumulation not only lead to an increased gain at the device edges but also modify the profile of the refractive index. Ultimately in both cases excitation of higher order lateral modes is supported. Furthermore as a consequence of longitudinal and lateral spatial hole burning depletion of carriers supporting lower order lateral modes and the resulting refractive index variations lead to transverse instabilities as well.

Laser simulation tools based on the solution of the full drift–diffusion equations [5, 7] treat the current flow in the device and its interaction with the non–equilibrium carrier densities in a correct manner. These models are based on a stationary approximation and use for the description of the optical field either an expansion into linear waveguide modes [5] or a beam propagation method [7]. However, the

DOI 10.20347/WIAS.PREPRINT.2488 Berlin 2018

applicability of both methods to BA lasers is questionable because of their inherent non–stationary and highly non–linear behavior. Indeed, these models do not converge at high optical output power, so that far–field blooming effects can be studied only slightly above threshold.

Hence for the simulation of BA lasers a time–dependent model has to be employed. Due to computer restrictions, until now simulation tools based on the traveling–wave model for the optical field [8, 9, 10] do not solve the time–dependent drift–diffusion equations, but only a lateral diffusion equation for the excess carriers in the active layer with a spatially constant injection current density below the contact stripe as source term. Such a constant–injection–current–density model, which is even used by stationary simulation tools [11, 12] oversimplifies the current flow and carrier transport in the device, because current spreading and current self–distribution are not taken into account [13]. An improved model can be gained from the drift–diffusion equations if recombination in the bulk layer is neglected and the conductivity in the n–doped region is assumed to be infinitely high (besides the common local charge neutrality assumption). The resulting Laplace equation for the quasi–Fermi potential of the holes in the p–doped region can be solved either approximately as proposed in Ref. [14] (Joyce model) or exactly [15, 16].

An advanced model coupling sophisticated descriptions of current flow, carrier transport, and guiding and propagation of the optical field is a powerful tool for the investigation of current and power dependent near– and far–field effects in BA lasers and for devive optimization. This is why in this paper we investigate the above mentioned models for the injection current density in BA lasers and their limits with respect to the correct description of non–thermal far field broadening. For that we have used the software kit BALaser [17], which solves the traveling wave equations for the optical field amplitudes coupled to an effective diffusion equation for the excess carrier density in the active region.

The paper is organized as follows: In Section 2 we present the governing model equations and parameters entering the model as well as the investigated device structure, where we pay particular attention to the assumptions made and the resulting equations for the carrier transport. In Section 3 we conduct a comparative study of the three models for the injection current density and will see that for all models a broadening of the far field with rising current is visible. Still, in Section 4 we will come to the conclusion that a constant injection current density can only be assumed for device structures where current spreading is small and the resistivity of the p–doped layers high. The Joyce model is a good approximation for structures with small current spreading and arbitrary resistivity of the p–doped layers. For structures where current spreading is large, however, the current injection density should be obtained by the solution of the Laplace problem, because otherwise far field broadening is underestimated.

2 Model

The structure of the BA laser considered in this paper is sketched in Fig. 1. Beside the 4 mm long and 90 μm broad contact stripe shallow index trenches are etched (effective index step $\Delta n_{\text{eff}} = 10^{-4}$).

2.1 Optical Model

For the simulation of the optical field the following ansatz is made for the electric component of the optical field:

$$\boldsymbol{E}(\boldsymbol{r},t) = \boldsymbol{e}_x \varphi(y) \frac{1}{2} \sqrt{\frac{2d\hbar\omega}{\epsilon_0 \bar{n} n_{\mathsf{g}}}} \left[u^+(x,z,t) \mathrm{e}^{-i\bar{n}k_0 z} + u^-(x,z,t) \mathrm{e}^{i\bar{n}k_0 z} \right] \mathrm{e}^{i\omega t} + c.c., \tag{1}$$

where d, $\hbar$, ϵ_0, n_g, $\bar{n}$ and ω are the thickness of the active region, the Planck constant, the vacuum permittivity, the group index, a real valued reference index, and a reference angular frequency, respectively. The dynamical simulation of the optical field coupled to injected charge carriers is carried out in the two–dimensional lateral–longitudinal (x, z)–plane of the active region (Fig. 1). The effective model parameters are calculated in advance from the given vertical (y–direction) epitaxial structure using the real–valued normalized vertical mode profile $\varphi(y)$ determined from the refractive index profiles of the respective layer structures in the different device areas. All model parameters are stepwise constant in the (x, z) plane and independent of time. Their values are shown in Table 1. The traveling wave equations for the complex slowly varying amplitudes $u^\pm(x, z, t)$ of the forward and backward traveling optical fields are defined in the longitudinal–lateral plane [18],

$$\frac{1}{v_\mathrm{g}}\partial_t u^\pm \pm \partial_z u^\pm = -\frac{i}{2\bar{n}k_0}\partial_x^2 u^\pm - i\Delta\beta u^\pm - \frac{g_r}{2}\left(u^\pm - p^\pm\right) + f_\mathrm{sp}^\pm, \tag{2}$$

where v_g, $k_0 = \omega/c$, and $f_\mathrm{sp}^\pm$ are the group velocity, the free space propagation constant, and a stochastic Langevin force modeling spontaneous emission, respectively. In (2) and in what follows ∂_z means partial differentiation with respect to the variable in the subscript (here z). A detailed derivation can be found in Ref. [19].

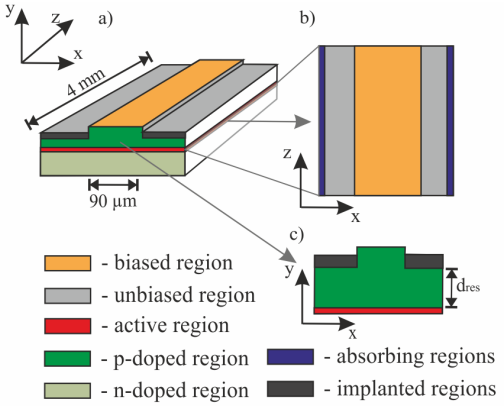

Figure 1: Schematic representation of the (a) simulated BA laser, (b) the longitudinal–lateral (x, z) and (c) the lateral–vertical plane of simulation. Active region: red–colored rectangular, implanted region: black.

The relative modal propagation constant is

$$\Delta\beta = k_0\Delta n_0 + k_0\Delta n_N + i(g - \alpha)/2. \tag{3}$$

Here, $\Delta n_0 = n_0 - \bar{n}$ with $n_0(x)$ denoting the effective index of the local vertical waveguide. Furthermore, $\Delta n_N = -\sqrt{n'_N N}$, where n'_N is the differential modal effective index. For the modal gain g we employ a logarithmic model taking into account non–linear gain compression,

$$g(N, ||u||^2) = \frac{g' \ln\left(\frac{\max(N,N_0)}{N_\mathrm{tr}}\right)}{1 + \epsilon_\mathrm{s}\|u\|^2}, \tag{4}$$

where g', N_0, N_tr, and ϵ_g are the differential modal gain, the gain clamping carrier density, the transparency carrier density, and the gain compression factor, respectively. $\|u\|^2 = |u^+|^2 + |u^-|^2$ denotes the local photon density. The modal absorption coefficient is calculated as $\alpha = \alpha_0 + \alpha_N$, with free–carrier absorption $\alpha_N = f_N N$ in the active region. The traveling wave equations are coupled to ordinary differential equations for the complex slowly varying amplitudes of the polarization fields $p^\pm$,

$$\partial_t p^\pm = \gamma(u^\pm - p^\pm) + i\delta\omega p^\pm, \tag{5}$$

which model the Lorentzian approximation of the material gain dispersion of the amplitude g_r, the half width at half maximum γ, and the relative central frequency $\delta\omega$. The parameters describing the dependence of gain or refractive index on carrier density as well as gain dispersion are obtained by a fit to results of a microscopic gain model [20].

Table 1: Parameters used in the simulation

symbol	parameter	value	unit
n_g	group refractive index	3.915	
$\bar{n}$	reference refractive index	3.422	
λ	central wavelength	$970 \cdot 10^{-9}$	m
r_0	front facet field amplitude reflectivity	$\sqrt{0.01}$	
r_L	rear facet field amplitude reflectivity	$\sqrt{0.95}$	
$\varphi_{0,L}$	phase of front and rear facet reflectivities	0	
d	thickness of active region	$7 \cdot 10^{-9}$	m
W	width of contact stripe	$90 \cdot 10^{-6}$	m
L	length of contact stripe	$4 \cdot 10^{-3}$	m
g'	differential modal gain	2300	m^{-1}
N_tr	transparency carrier density	$1.7 \cdot 10^{24}$	m^{-3}
N_0	gain clamping carrier density	$4 \cdot 10^{23}$	m^{-3}
ε_s	gain compression factor	10^{-24}	m^3
g_r	amplitude of Lorentzian	4500	m^{-1}
γ	Lorentzian half width at half maximum	$1.5 \cdot 10^{13}$	s^{-1}
$\delta\omega$	detuning of Lorentzian	0	s^{-1}
α_0	internal background absorption	40	m^{-1}
f_N	modal cross section for free carrier absorption	$2.1 \cdot 10^{-23}$	m^2
r_s	series resistivity related to contact layer	$5 \cdot 10^{-9}$	$\Omega\mathsf{m}^2$
Ω	sheet resistance		
	for $d_\mathsf{res} = 1215$ nm (large current spreading)	1.2	$\mathsf{k}\Omega$
	for $d_\mathsf{res} = 770$ nm (reduced current spreading)	8	$\mathsf{k}\Omega$
Δn_0	built–in relative effective index		
	for $(x, z) \in$ index trench	$-1 \cdot 10^{-4}$	
	for $(x, z) \notin$ index trench	0	
n'_N	differential modal effective index	$4 \cdot 10^{-31}$	m^3
E_g	band gap energy	1.28	eV
N_c	conduction band density of states	$0.97 \cdot 10^{24}$	m^{-3}
N_v	valence band density of states	$4.66 \cdot 10^{24}$	m^{-3}
μ_p	hole mobility in active region	$300 \cdot 10^{-4}$	$\mathsf{m}^2(\mathsf{Vs})^{-1}$
A	Shockley Read Hall recomb. coefficient	$9.09 \cdot 10^8$	s^{-1}
B	spontaneous emission recomb. coefficient	$1 \cdot 10^{-16}$	$\mathsf{m}^3\mathsf{s}^{-1}$
C	Auger recomb. coefficient	$2 \cdot 10^{-42}$	$\mathsf{m}^6\mathsf{s}^{-1}$

2.2 Carrier Transport Model

As the device is longitudinally much further extended than laterally, longitudinal carrier transport plays a minor role and we will restrict our study to vertical–lateral carrier transport only [21]. Under isothermal conditions the carrier transport is commonly described by a drift diffusion model, which was first established by van Roosbroeck. The electric field is affected by the charge distribution of mobile (n and p) and fixed (n_A and p_D) charges, thus for the electrostatic potential ϕ,

$$-\nabla(\epsilon\nabla\phi) = e(p - n + p_D - n_A), \tag{6}$$

holds, where ϵ is the dielectric constant. In all layers charge neutrality is assumed,

$$p - n + p_D - n_A = 0. \tag{7}$$

The mobile charges $n = n_0 + N$ and $p = p_0 + N$ are composed of equilibrium carrier densities n_0 and p_0 and an excess carrier density N. The particle current flow is governed by the continuity equations for electrons and holes,

$$\nabla \boldsymbol{j}_n = e\left(R + R_{\text{stim}} + \partial_t n\right), \tag{8}$$
$$-\nabla \boldsymbol{j}_p = e\left(R + R_{\text{stim}} + \partial_t p\right), \tag{9}$$

with the current densities for electrons and holes, $\boldsymbol{j}_n$ and $\boldsymbol{j}_p$, the non–radiative and spontaneous radiative recombination rate R and the stimulated recombination rate R_{stim}.

For parabolic bands the current densities can be written as product of the conductivity for electrons and holes, $\sigma_n = e\mu_n n$, and $\sigma_p = e\mu_p p$, where μ_n and μ_p are the electron and hole mobility, and the gradient of the quasi Fermi–potentials φ_n and φ_p,

$$\boldsymbol{j}_n = -\sigma_n\nabla\varphi_n, \tag{10}$$
$$\boldsymbol{j}_p = -\sigma_p\nabla\varphi_p. \tag{11}$$

The Fermi integral of order one–half $F_{1/2}$ connects the carrier densities n and p and the effective densities of states N_{c} and N_{v} with the exponents of the Fermi function $(e\varphi_n + e\phi - E_{\text{c}})/k_{\text{B}}T$ and $(E_{\text{v}} + e\varphi_p - e\phi)/k_{\text{B}}T$ [22],

$$\frac{n}{N_{\text{c}}} = F_{1/2}\left(\frac{e\phi - e\varphi_n - E_{\text{c}}}{k_{\text{B}}T}\right) \quad \text{or} \quad \frac{p}{N_{\text{v}}} = F_{1/2}\left(\frac{E_{\text{v}} + e\varphi_p - e\phi}{k_{\text{B}}T}\right), \tag{12}$$

where φ_n and φ_p are the electrochemical potentials of electron and holes and E_{c} and E_{v} conduction and valence band edge energies. The Fermi potential will be calculated in the Joyce–Dixon approximation. [23] The electron and hole current flow can furthermore be separated into parts driven by drift and diffusion,

$$\boldsymbol{j}_n = n\mu_n\nabla(E_{\text{c}} - e\phi) + eD_n\nabla n \tag{13}$$
$$\boldsymbol{j}_p = p\mu_p\nabla(E_{\text{v}} - e\phi) - eD_p\nabla p \tag{14}$$

with the concentration dependent diffusion coefficient for electrons D_n and holes D_p,

$$D_n = \mu_n\frac{k_{\text{B}}T}{e}\frac{n}{N_{\text{c}}}F_{1/2}^{-1'}\left(\frac{n}{N_{\text{c}}}\right) \quad \text{and} \quad D_p = \mu_p\frac{k_{\text{B}}T}{e}\frac{p}{N_{\text{v}}}F_{1/2}^{-1'}\left(\frac{p}{N_{\text{v}}}\right), \tag{15}$$

where $F_{1/2}^{-1'}$ is the derivative of the inverse Fermi integral of order one–half $F_{1/2}$.

One of the basic assumptions is that the electron conductivity in the n–doped region is much larger than the hole conductivity in the p–doped region. Hence, by assuming $\sigma_n \to \infty$ it follows $\nabla\varphi_n \to 0$ so that

$$\varphi_n \approx \text{const.} = 0 \tag{16}$$

can be set. As a consequence the electron current $\boldsymbol{j}_n$ is composed only of a vertical component $j_{n,y}$, that remains constant in vertical direction.

2.2.1 Carrier transport in the active region

Within the active region the carrier density is given by the excess carrier density N. Following *W. B. Joyce* [24] an equation for the lateral carrier transport within the active region is derived, which is considered to be thin enough so that vertical carrier transport can be averaged over.
Considering (16) and inserting (15) into (13) we obtain

$$\partial_x \left(\frac{E_\mathsf{c}}{e} - \phi \right) = -\partial_x \left(\frac{k_\mathsf{B}T}{e} F_{1/2}^{-1} \left(\frac{n}{N_\mathsf{c}} \right) \right) \tag{17}$$

We exploit the parallelism of band edges ($\nabla E_\mathsf{c} = \nabla E_\mathsf{v}$) and insert (17) into (14) to obtain an equation for the lateral current density,

$$j_{p_x} = -\sigma_p \partial_x \left(\frac{k_\mathsf{B}T}{e} F_{1/2}^{-1} \left(\frac{n}{N_\mathsf{c}} \right) \right) - \sigma_p \partial_x \left(\frac{k_\mathsf{B}T}{e} F_{1/2}^{-1} \left(\frac{p}{N_\mathsf{v}} \right) \right). \tag{18}$$

With the definition of the Fermi integral (12) we obtain,

$$\begin{aligned} j_{p_x} &= -\sigma_p \partial_x \left(-\varphi_n - E_\mathsf{c}/e + \phi + E_\mathsf{v}/e - \phi + \varphi_p \right) && (19)\\ &= -\sigma_p \partial_x (\varphi_p - \varphi_n) = -\sigma_p \partial_x \varphi_F && (20)\\ &= -eD_\mathsf{eff} \partial_x N && (21) \end{aligned}$$

with an effective diffusion coefficient $D_\mathsf{eff} = \sigma_p \partial_N \varphi_F / e$ and conductivity $\sigma_p = e\mu_p(p_0 + N)$. Inserting (21) into the continuity equation for the holes (9) gives,

$$\partial_t N = \partial_x \left(D_\mathsf{eff} \partial_x N \right) - \frac{\partial_y j_{p_y}}{e} - R - R_\mathsf{stim}. \tag{22}$$

Averaging (22) across the active region with thickness d and neglecting the vertical hole leakage current, which is well valid due to low hole mobility and usually high potential barriers, yields

$$\partial_t N = \partial_x (D_\mathsf{eff} \partial_x N) + \frac{j}{ed} - R - R_\mathsf{stim}, \tag{23}$$

where $j = -j_{p_y}|_{\text{upper boundary of AR}}$, $R(N) = AN + BN^2 + CN^3$, and $R_\mathsf{stim} = v_\mathsf{g}\mathsf{Re} \sum_{\nu=\pm} u^{\nu *}[gu^\nu - g_r(u^\nu - p^\nu)]$. The coefficients A for Shockley–Read–Hall, B for spontaneous radiative and C for Auger recombination are standard values taken from literature, which are validated by a fit of simulation results to cavity length dependent experimental data. The desired hole injection current density $j(N)$ at the upper boundary of the active region can be calculated by different models as described in the following section.

2.2.2 Models for the injection current

Due to assumption of an infinite electron conductivity in the n–doped region, only the current flow in the p–doped region sketched in Fig. 1(c) needs to be considered. The lower boundary is given by the upper boundary of the active region (marked red in Fig. 1(c)). The upper boundary is defined by the metal contact in the center and the lower boundaries of adjacent regions with a vanishing conductivity (marked black in Fig. 1(c)). Such regions for current confinement can be created by e.g. implantation, diffusion or impurity induced disordering. The distance between the upper boundary of the active region and the lower boundary of the implanted region is denoted by the residual layer thickness d_{res}.

By neglecting recombination in the bulk layers, the drift–diffusion equation in the p–doped layer (9) results in

$$\nabla \boldsymbol{j}_p = 0. \tag{24}$$

By inserting (11) we obtain the Laplace equation for the hole Fermi potential,

$$\nabla(\sigma_p \nabla \varphi_p) = 0. \tag{25}$$

At the upper metal contact the potential is given by the applied voltage $\varphi_p = U_0$, at the lower boundary to the active region the potential is given by the Fermi potential $\varphi_p = \varphi_F$. At all other device boundaries the derivative of the electrochemical potential normal to the device surface vanishes, $\partial_n \varphi_p = 0$. In the Laplace model the injection current density entering (23) is accordingly given by

$$j(x) = \sigma_p \partial_y \varphi_p \qquad \text{at the boundary to the active region.} \tag{26}$$

The Joyce model [14] is based on an approximate solution of the Laplace equation for the quasi–Fermi potential of the holes in the p–doped region and describes the injection current density as

$$j(x) = \begin{cases} (U - \varphi_F)/r_{\text{s}} & \text{below the contact stripe} \\ \partial_x^2 \varphi_F / \Omega & \text{beside the contact stripe,} \end{cases} \tag{27}$$

where $r_{\text{s}} = \int_{\text{p-layers}} [\sigma_p(y)]^{-1} dy$ is the series resistance related to the contact area and $\Omega = [\int_{\text{p-layers}} \sigma_p(y) dy]^{-1}$ is the sheet resistance. Layer thicknesses and conductivities are given in Table 2, the corresponding values of r_{s} and Ω in Table 1. Further details on the device structure are given in another publication. [25]

Table 2: Layer thicknesses and conductivities

	thickness	conductivity
contact layer	130 nm	$26680\ (\Omega\text{m})^{-1}$
cladding layer	445 nm	$1660\ (\Omega\text{m})^{-1}$
confinement layer	770 nm	$163\ (\Omega\text{m})^{-1}$

The model of a spatially constant current injection density j_{const} used by many simulation tools is given by

$$j(x) = \begin{cases} j_0 & \text{below the contact stripe} \\ 0 & \text{beside the contact stripe.} \end{cases} \tag{28}$$

Note that (28) is a limit case of (27) for $r_{\text{s}} \to \infty$ and $\Omega \to \infty$.

3 Comparison of Models for Injection current density

The calculation shown in Fig. 2 was performed with a staircase voltage ramp. The total simulation time for each stair is 5 ns, all values derived in this paper are calculated from the mean value of the last nanosecond.

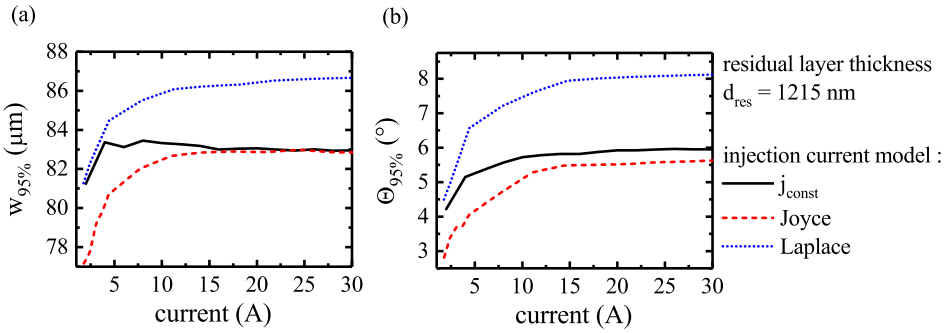

Figure 2: (a) Full lateral near field width $w_{95\%}$ and (b) full far field angle $\Theta_{95\%}$ containing 95% of the power as function of the total injection current for different models for the injection current density: constant injection current density (black), Joyce model (red dashed) and by solution of the Laplace equation (blue dotted). The residual layer thickness is $d_{\text{res}} = 1215$ nm, corresponding to a sheet resistance of $\Omega = 1.2$ kΩ.

In Fig. 2 the full lateral near field width $w_{95\%}$ and full far field angle $\Theta_{95\%}$ containing 95% of the power are shown as function of total injection current for the different current injection density models discussed in Section 2.2.2. The simulation was performed for a residual layer thickness of $d_{\text{res}} = 1215$ nm, which corresponds to a sheet resistance of $\Omega = 1.2$ kΩ and results in a large spreading current. For all models a widening of near and far field is visible, however, the far field broadening is lowest when a constant injection current density j_{const} is assumed. When the Joyce model is employed near and far field width are much smaller for injection currents up to 10 A compared to the results with a constant injection current density or by solution of the Laplace problem. As a result at a high injection current of 20 A the near field width has a value of $w_{95\%} = 86.5$ μm and the far field angle a value of $\Theta_{95\%} = 8°$ when the Laplace problem is solved, resulting in a beam parameter product of $\text{BPP}_{\text{lat}} = w_{95\%}\Theta_{95\%}/4 = 3$ mm·mrad. On the contrary, we obtain a near field width of $w_{95\%} = 83$ μm when the Joyce model or a constant injection current density are employed and a far field angle of $\Theta_{95\%} = 5.5°$ or $6°$ when the Joyce model or a constant injection current density are used, respectively, resulting in a beam parameter product of $\text{BPP}_{\text{lat}} \approx 2$ mm · mrad. Accordingly the near field width $w_{95\%}$ is underestimated by 4% and the far field angle $\Theta_{95\%}$ by 25 to 30%, which leads to an underestimation of the beam parameter product BPP_{lat} by more than 30%.

For a residual layer thickness of $d_{\text{res}} = 1215$ nm, the profiles of carrier density, injection current density, as well as near and far field profiles are displayed in Fig. 3 at a very high injection current of 20 A. In Fig. 3(b) we can observe that a simulation with the Joyce model results in peaks of the current injection density at the stripe edges. For the Laplace model a higher carrier density is visible outside the injection stripe at $x < -45$ μm and $x > 45$ μm compared to the other models (Fig.3(a)) which is a result of larger current spreading (Fig.3(b)). This carrier density variation results in a gain and refractive index modification and finally in a broader near (Fig.3(c)) and far (Fig.3(d)) field. For a residual layer thickness of $d_{\text{res}} = 770$ nm, the full lateral near field width $w_{95\%}$ and full far field angle

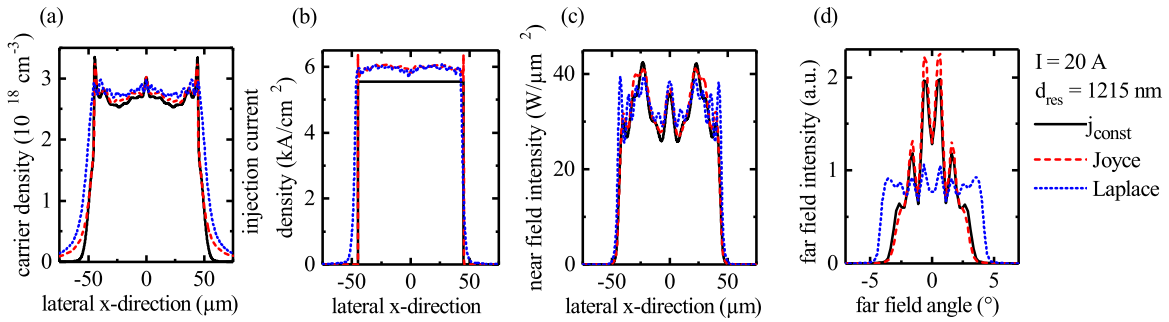

Figure 3: Profiles of the (a) carrier density, (b) injection current density and (c) near field intensity as function of the lateral coordinate at the output facet and (d) the far field intensity as function of the lateral far field angle for an injection current of 20 A and a residual layer thickness of $d_{\text{res}} = 1215$ nm.

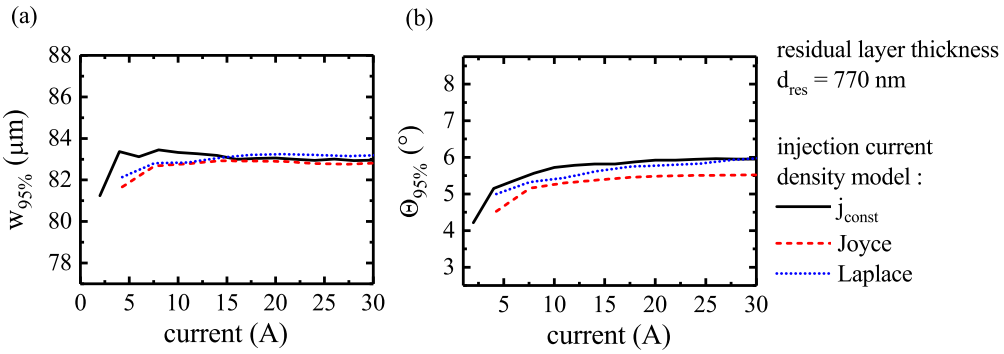

Figure 4: (a) Full lateral near field width $w_{95\%}$ and (b) full far field angle $\Theta_{95\%}$ containing 95% of the power as function of the total injection current for different models for the injection current density: constant injection current density (black), Joyce model (red dashed) and by solution of the Laplace equation (blue dotted). The residual layer thickness is $d_{\text{res}} = 770$ nm, corresponding to a sheet resistance of $\Omega = 8$ kΩ.

$\Theta_{95\%}$ is plotted in Fig. 4 as function of total injection current for the different current injection density models. The residual layer thickness of $d_{\text{res}} = 770$ nm corresponds to a sheet resistance of 8 kΩ and results in reduced current spreading. In this case a slight widening of the far field is visible for all models, as well. However, only minor differences in near and far field width are visible for the different models. The same applies for the profiles of carrier density, injection current density, and near and far field displayed in Fig. 5 for an injection current of 20 A. In Fig. 5(a) we see that the carrier density distribution is nearly identical when the Joyce model is used or the Laplace problem is solved. Hole burning is slightly higher for the simulation where a constant injection current density was assumed due to overestimation of spatial holeburning. Still, as the series resistivity $r_{\text{s}} = 5 \cdot 10^{-9}$ Ωm^2 of the simulated structure is relatively high, the deviation from the simulation with a constant injection current density is small. As a result, the profiles of near and far field are nearly identical.

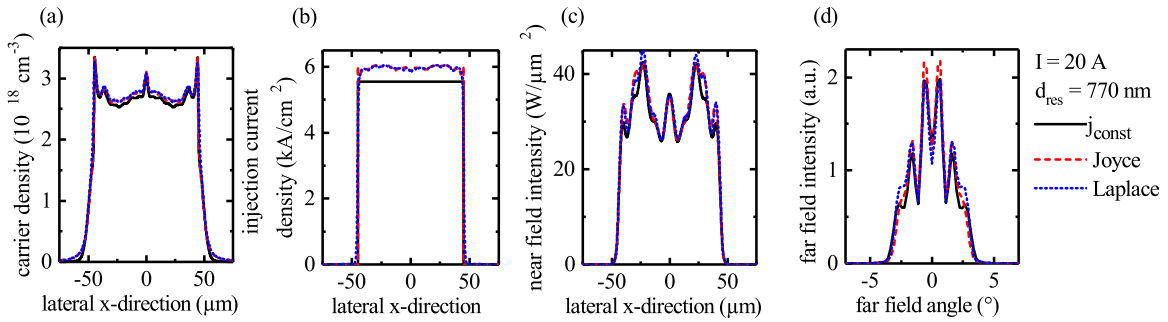

Figure 5: Profiles of the (a) carrier density, (b) injection current density and (c) near field intensity as function of the lateral coordinate at the output facet and (d) the far field intensity as function of the lateral far field angle for an injection current of 20 A and a residual layer thickness of $d_{\text{res}} = 770$ nm.

4 Conclusion & Outlook

For all models a broadening of the far field with rising current is visible. However, when a constant injection current density is assumed spatial holeburning is overestimated and current spreading not accounted for. Thus a constant injection current density can only be assumed for device structures where current spreading is small and the resistivity of the p–doped layers large. The Joyce model is a good approximation for structures with small current spreading and arbitrary resistivity of the p–doped layers. For structures where current spreading is high, however, the current injection density should be obtained by the solution of the Laplace problem, because otherwise the far field angle will be underestimated. In this paper we exemplary show for a specific device structure that the near field width is underestimated by 4 % and the far field angle by 25 to 30 % if the simplified models are employed, resulting in an overestimation of the beam quality, where the beam parameter product BPP is underestimated by more than 30%. The impact of series resistivity and sheet resistance on the lateral near field width and far field angle will be analyzed in a forthcoming paper [26].

Acknowledgments

This work is supported by the German Federal Ministry of Education and Research contract 13N14005 as part of the EffiLAS/HotLas project.

References

[1] Wenzel, H., Crump, P., Ekhteraei, H., Schultz, C., Pomplun, J., Burger, S., Zschiedrich, L., Schmidt, F., and Erbert, G., “Theoretical and experimental analysis of the lateral modes of high-power broad–area lasers,” *Proc. NUSOD* , 10–11 (2011).

[2] Crump, P., “Experimental and theoretical analysis of the dominant lateral waveguiding mechanism in 975 nm high power broad area lasers,” *Semicond. Sci. Technol.* **27**, 045001 (2012).

[3] Piprek, J., “Self-consistent far–field blooming analysis for high-power Fabry–Perot laser diodes,” *Proc. SPIE* **8619**, 861910 (2013).

[4] Rauch, S., Wenzel, H., Radziunas, M., Haas, M., Tränkle, G., and Zimer, H., "Impact of longitudinal refractive index change on the near–field width of high-power broad–area diode lasers," *Appl. Phys. Lett.* **110**(26), 263504 (2017).

[5] Piprek, J. and Simon Li, Z. M., "On the importance of non–thermal far-field blooming in broad–area high-power laser diodes," *Appl. Phys. Lett.* **102**(221110), 1–4 (2013).

[6] Winterfeldt, M., Crump, P., Knigge, S., Maaßdorf, A., Zeimer, U., and Erbert, G., "High beam quality in broad area lasers via suppression of lateral carrier accumulation," *IEEE Photon. Techn. Lett.* **27**(17), 1809–1812 (2015).

[7] Borruel, L., Sujecki, S., Moreno, P., Wykes, J., Krakowski, M., Sumpf, B., Sewell, P., Auzanneau, S.-C., Wenzel, H., Rodríguez, D., et al., "Quasi-3-D simulation of high-brightness tapered lasers," *IEEE J. Quantum Electron.* **40**(5), 463–472 (2004).

[8] Ning, C., Indik, R., and Moloney, J., "Effective bloch equations for semiconductor lasers and amplifiers," *IEEE J. Quantum Electron.* **33**(9), 1543–1550 (1997).

[9] Lichtner, M., Radziunas, M., Bandelow, U., Spreemann, M., and Wenzel, H., "Dynamic simulation of high brightness semiconductor lasers," *Proc. NUSOD '08* , 65–66 (2008).

[10] Pérez-Serrano, A., Javaloyes, J., and Balle, S., "Spectral delay algebraic equation approach to broad area laser diodes," *IEEE J. Sel. Topics Quantum Electron.* **19**(5), 1–8 (2013).

[11] Eckstein, H.-C. and Zeitner, U. D., "Modeling electro-optical characteristics of broad area semiconductor lasers based on a quasi–stationary multimode analysis," *Optics express* **21**(20), 23231–23240 (2013).

[12] Holly, C., Hengesbach, S., Traub, M., and Hoffmann, D., "Simulation of spectral stabilization of high–power broad-area edge emitting semiconductor lasers," *Optics express* **21**(13), 15553–15567 (2013).

[13] Eliseev, P., Glebov, A., and Osinski, M., "Current self–distribution effect in diode lasers: analytic criterion and numerical study," *IEEE J. Sel. Topics Quantum Electron* **3**(2), 499–506 (1997).

[14] Joyce, W. B., "Current–crowded carrier confinement in double–heterostructure lasers," *J. Appl. Phys.* **51**(53), 2394–7235 (1980).

[15] Hadley, G. R., Hohimer, J. P., and Owyoung, A., "Comprehensive modeling of diode arrays and broad-area devices with applications to lateral index tailoring," *IEEE J. Quantum Electron.* **24**(11), 2138–2152 (1988).

[16] Niederhoff, M., Heinrich, W., and Russer, P., "Three-dimensional modelling of high-power laser diodes based on the finite integration beam propagation method," *IEEE MTT-S Intern. Microwave Symp. Dig.* **3**, 1429–1432 (1996).

[17] BALaser, "A software tool for simulation of dynamics in broad area semiconductor lasers. http://www.wias-berlin.de/software/balaser/."

[18] Radziunas, M. and Ciegis, R., "Effective numerical algorithm for simulations of beam stabilization in broad area semiconductor lasers and amplifiers," *Mathematical Modelling and Analysis* **19**(5), 627–646 (2014).

[19] Wenzel, H. and Zeghuzi, A., "High power lasers," in [*Handbook of Optoelectronic Device Modeling and Simulation: Lasers, Modulators, Photodetectors, Solar Cells, and Numerical Methods-Volume Two*], Piprek, J., ed., ch. 27, CRC Press (2017).

[20] Wenzel, H., Erbert, G., and Enders, P. M., "Improved theory of the refractive–index change in quantum–well lasers," *IEEE J. Sel. Topics Quantum Electron.* **5**(3), 637–642 (1999).

[21] Radziunas, M., Zeghuzi, A., Fuhrmann, J., Koprucki, T., Wünsche, H.-J., Wenzel, H., and Bandelow, U., "Efficient coupling of inhomogeneous current spreading and dynamic electro–optical models for broad–area edge–emitting semiconductor devices," *Opt. Quant. Electron.* **49**, 332/1–332/8 (2017).

[22] Coldren, L. A., Corzine, S., and Masanovic, M. L., [*Diode Lasers and Photonic Integrated Circuits*], Wiley, 2nd ed. (2012).

[23] Joyce, W. B. and Dixon, R. W., "Analytic approximations for the Fermi energy of an ideal Fermi gas," *Appl. Phys. Lett.* **31**(5), 354–356 (1977).

[24] Joyce, W. B., "Carrier transport in double-heterostructure active layers," *J. Appl. Phys.* **53**(11), 7235–7239 (1982).

[25] Crump, P., Erbert, G., Wenzel, H., Frevert, C., Schultz, C. M., Hasler, K.-H., Staske, R., Sumpf, B., Maassdorf, A., Bugge, F., Knigge, S., and Tränkle, G., "Efficient high-power laser diodes," *IEEE J. Sel. Topics Quantum Electron.* **19**(4), 1–11 (2013).

[26] Zeghuzi, A., Radziunas, M., Wenzel, H., Wünsche, H.-J., Bandelow, U., and Knigge, A., "Impact of current spreading and p-layer resistivity on the lateral beam quality of broad area lasers," *Appl. Phys. Lett.* (to be submitted 2018).